Simulating and Optimizing Nasopharyngeal Swab Insertion Paths for use in Robotics

Peter Q. Lee[1], John S. Zelek and Katja Mombaur

***Abstract*— The nasopharyngeal swab is the standardized method of collecting specimens for diagnosing COVID-19, among numerous other respiratory illnesses. While there has been interest from the robotics community in the design of robots and manipulators for performing swab collections, detailed simulation and planning for swab insertion trajectories through the nasal cavity is less studied. In this work, we propose a simulation environment with the swab modelled as an Euler-Bernoulli beam, subject to linear elastic collisions coming from the nasal cavity. We evaluate the impact of inserting the swab with different amounts of force. We also leverage the simulation environment to pose an optimization problem that finds trajectories that minimize strain on the swab during the insertion. We find that the optimized trajectories adhere to qualitative clinical advice.**

I. Introduction

The Polymerase chain reaction (PCR) test via nasopharyngeal swab (NPS) specimen is currently well known as the gold-standard method for diagnosing COVID-19 [1] [2], in addition to being a standardized method for diagnosing many other types of diseases, including various strains of coronavirus, influenza, whooping cough, pneumonia, and rhinovirus [3]. The procedure of NPS specimen collection is to insert a flocked swab through the nasal cavity and collect samples from the nasopharynx [4]. The anatomy of the nasal cavity provides a number of challenges in terms of geometry. The swab has to navigate through the nasal cavity and requires an angle of insertion that can reach the nasopharynx, while also avoiding becoming wedged on the turbinates in the nasal cavity. The swab also cannot be visually observed once it is inserted; thus the healthcare worker must be guided entirely on prior knowledge and tactile feedback.

Currently, most instructions for obtaining NPS specimens are based on qualitative instructions given to healthcare workers that can vary significantly between different health authorities [5]. Piras *et al.* [4] suggest inserting the swab with a pitch angle that is parallel to the palate at a distance equivalent from the nostril to the ear, but do not provide any yaw angle instructions. Marty *et al.* [6] provide similar insertion strategies. In correspondence [7], one reviewer suggested that the swab should be directed from the nostril towards the earlobe, although it is not clear if this was a suggestion for yaw orientation or if it was solely meant as pitch guidance.

Generally NPS collection consists of three of distinct phases, as shown in Figure 1. First, the swab is inserted through the nasal cavity until it reaches nasopharynx. Second, the swab is rotated to collect a specimen at the nasopharynx. Third, the swab is extracted and prepared for storage. This paper will solely focus on the insertion phase, where we will study the best way to insert the swab through the nasal cavity in a quantitative manner.

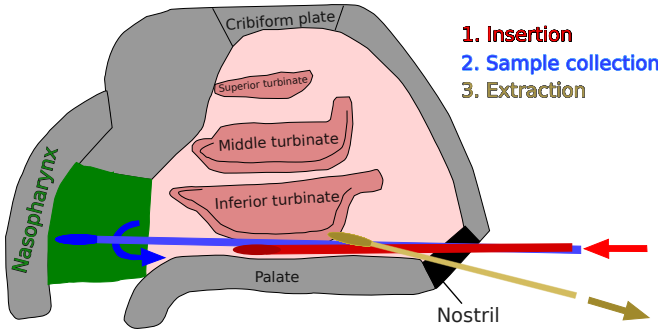

Fig. 1: The three stages of a nasopharyngeal swab collection. This paper will be focusing on the first; the insertion stage.

An overarching topic that is of rising interest is the application of robots in close-contact healthcare tasks, such as NPS tests, as a way to protect human healthcare workers from the risk of infection posed by their patients [8]. Robots can also ease the burden of the healthcare system during labour disruptions or during health crises. The COVID-19 pandemic in particular has spawned several recent works concerning robots performing swab tests. Zhang *et al.* [9] designed a remote centre compliance manipulator with a vision and force controlled system to perform oropharyngeal swab tests through the open mouth. Wang *et al.* [10] designed a custom end-effector that fits a swab that applies linear actuation and rotation along the axis of insertion towards the nasopharynx. Axial displacement of the swab is read by an optoelectronic sensor to measure force in the axis of the insertion. Currently, there is a deficiency in the literature towards planning or simulating insertion trajectories of the swab through the nasal cavity. From the standpoint of medical robotics, the study of these insertion trajectories will be an essential step towards planning and executing NPS tests on patients.

There are, however, a variety of other tasks in robotics that share some characteristics. Like a swab, a needle can also be characterized as a long, slender beam that shares the characteristic of deforming under pressure [11]. Needle insertion models can account for the tissue force response with a variety of a different linear elastic or viscoelastic

Peter Q. Lee, John Zelek, and Katja Mombaur are with the Department of Systems Design Engineering, Faculty of Engineering, University of Waterloo, Ontario, Canada {pqjlee, jzelek, katja.mombaur}@uwaterloo.ca

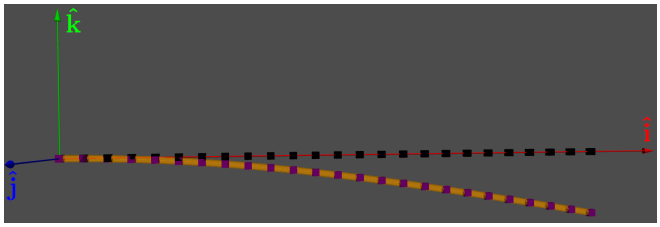

Fig. 2: Visualization of beam, in orange, aligned to axis $\hat{\mathbf{i}}$ that is deformed along axis $\hat{\mathbf{k}}$. The purple cubes are the finite elements displaced from their reference positions in black.

models [12]. However, it should be noted that the contact physics differ between a swab and needle in significant ways. Namely, a needle actively penetrates tissue, whereas a swab does not; and a needle generally has a well defined contact phase, while a swab has multimodal contact phases due to the geometry of the nose. Peg-in-hole tasks share a similar objective of inserting an object into a receptacle while minimizing reaction forces from contact. Nonetheless, most peg-in-hole works are based on the assumptions of rigid body contacts with well-defined contact phases [13] so that most new developments are made towards online control and state-estimation rather than planning [14].

With this context, the contribution of this work is the following:

1) Formulate a simulation framework to model the motion and deformation of a swab as it is inserted into the nasal cavity (section II);
2) Derive a trajectory optimization problem to find ways to insert the swab into the nasal cavity in a manner that minimizes the amount of potential energy caused by the swab deforming, as a proxy for minimizing patient discomfort (section III); and
3) Analyze what paths through the nasal cavity are feasible in terms of reaching the nasopharynx and the accumulated amounts of potential energy (section IV).

In this initial work, the above contributions assume insertion through the average nasal cavity shape from Keustermans *et al.* [15] , with the intention of extending the analysis to a wider distribution of shapes in future work.

II. Simulation

The two main components of the simulation consist of the swab deformation and the collision response between the swab and the nasal cavity. We model the swab as a cantilevered beam whose base can translate along a reference axis. For the collision response we consider a linear elastic model with Coulomb friction.

A. Beam dynamics

The mechanics of beams have been well studied in a variety of fields. The most basic beam model is the Euler-Bernoulli beam, which models 3D deformations with five degrees of freedom related to deformation along the axis it is aligned with and the two perpendicular axes [16]. Other beam models exist, such as Timoshenko beams, which add degrees of freedom to account for shearing [17]. Nasopharyngeal swabs are thin compared to its length; following experiments from Zohoor and Kakavand [18], it is reasonable to use an Euler-Bernoulli model over more complicated models to reduce computational complexity. The beam has axis $\hat{\mathbf{i}}$ aligned to its reference state, with transverse axes $\hat{\mathbf{j}}$ and $\hat{\mathbf{k}}$. Hence, the deformation of the beam can be described by the displacement vector $\chi(x) = u(x)\hat{\mathbf{i}}+v(x)\hat{\mathbf{j}}+w(x)\hat{\mathbf{k}}$ given x as the position of the undeformed beam on axis $\hat{\mathbf{i}}$. The degrees of freedom of the beam are taken as $s, v, w, \phi = \frac{\partial v}{\partial x}, \theta = \frac{\partial w}{\partial x}$, where s is the axial strain, while the independent transverse deformation variables are v and w, along with their spatial derivatives ϕ and θ. To conserve the total length of the beam $u(x) = s(x) - h_v(x) - h_W(x)$, where $h_v = \int_0^x (\frac{\partial v}{\partial x})^2 d\xi$, $h_w = \int_0^x (\frac{\partial w}{\partial x})^2 d\xi$.

In this paper, we will consider a simplified control scenario where the swab is grasped at one end and moved along a single axis, $\hat{\mathbf{i}}$. Such a scenario would be amenable to a robot inserting the swab by applying a constant force along $\hat{\mathbf{i}}$, while restricting motion in the transverse axes. These assumptions will allow us to later evaluate insertion paths through the nasal cavity, while keeping the degrees of freedom low. Zohoor and Kakavand [18] derived a set of partial differential equations to describe the deformation of a cantilevered beam with a non-fixed support, which we modify to our scenario by removing terms describing motion of the base that are not along $\hat{\mathbf{i}}$ and by adding damping terms:

$$\begin{aligned}&\rho A\left(\ddot{s} - \left(\ddot{h}_v + \ddot{h}_w\right)\right) - EA\frac{\partial^2 s}{\partial x^2} \\ &= -\rho A(\ddot{x}_0) + F_u(x) + \alpha\dot{s},\end{aligned} \tag{1}$$

$$\begin{aligned}&\rho A\left(\ddot{v} - \frac{\partial}{\partial x}\frac{\partial v}{\partial x}\int_L^x \left[\ddot{x}_0 + \ddot{s} - \ddot{h}_v - \ddot{h}_w\right] d\xi\right) \\ &+ EI_z\left(\frac{\partial^4 v}{\partial x^4}\right) = F_v(x) + \alpha\dot{v},\end{aligned} \tag{2}$$

$$\begin{aligned}&\rho A\left(\ddot{w} - \frac{\partial}{\partial x}\frac{\partial w}{\partial x}\int_L^x \left[\ddot{x}_0 + \ddot{s} - \ddot{h}_v - \ddot{h}_w\right] d\xi\right) \\ &+ EI_y\left(\frac{\partial^4 w}{\partial x^4}\right) = F_w(x) + \alpha\dot{w},\end{aligned} \tag{3}$$

where x_0 is the base position (i.e., the grasp point), and hence $\ddot{x}_0$ is the acceleration of the base. We assume that the swab is a perfect cylinder, so that the cross sectional area $A = \frac{1}{2}\pi r^2$, and area moments of inertia $I_y = I_z = \frac{1}{3}\pi r^3$. The swab's radius $r = 1$ mm, Young's modulus $E = 3\times10^9$ Pa, damping coefficient $\alpha = 10^{-2}$, and material density $\rho = 640$ kg m^{-3} are defined based on the swab shaft being made of polystyrene.

Following Chung and Yoo [19] and Zohoor and Kakavand [18], these partial differential equations are linearized and discretized for simulation using a finite element modelling (FEM) strategy. This divides the beam into N evenly spaced nodes, as visualized in Figure 2. The continuous deformation is interpolated with polynomial basis functions between these nodes. Given a pair of nodes i and $i+1$ located at x_i and x_{i+1}, given $\hat{x} = x - x_i$ and $l = L/(N-1)$, then

the deformations are:

$$\begin{aligned} s(x) &= (1-\frac{\hat{x}}{l})s_i + \frac{\hat{x}}{l}s_{i+1} \\ v(x) &= \begin{bmatrix} v_i, & \phi_i, & v_{i+1}, & \phi_{i+1} \end{bmatrix} h(\hat{x})^\top \\ w(x) &= \begin{bmatrix} w_i, & \theta_i, & w_{i+1}, & \theta_{i+1} \end{bmatrix} h(\hat{x})^\top \\ h(\hat{x}) &= [1 - \frac{3\hat{x}^2}{l^2} + \frac{2\hat{x}^3}{l^3}, x - \frac{2\hat{x}^2}{l} + \frac{\hat{x}^3}{l^2}, \\ &\quad \frac{3\hat{x}^2}{l^2} - \frac{2\hat{x}^3}{l^3}, -\frac{\hat{x}^2}{l} + \frac{\hat{x}^3}{l^2}]. \end{aligned} \tag{4}$$

The weak-formulation of equations 1 to 3 become a second order ODE system

$$\overline{M}\ddot{\kappa} + \overline{D}\dot{\kappa} + \overline{\Lambda}\kappa = \overline{\Pi F} + \Omega\ddot{x}_0, \tag{5}$$

where $\overline{M}$, $\overline{D}$, $\overline{\Lambda}$, Ω, and $\overline{\Pi}$ are mass, damping, stiffness, acceleration, and force matrices found by summing equations 1 to 3, integrating, factoring the variables, and assembling. Also, we take $\kappa = \{s_2, v_2, \phi_2, w_2, \theta_2, \cdots, s_N, v_N, \phi_N, w_N, \theta_N\}$. To match our control scenario of applying constant force f_a in the $\hat{\mathbf{i}}$ direction, we take the base position x_0 into the state-space and refactor the matrices as

$$\begin{aligned} M &= \begin{bmatrix} \frac{\rho A l}{2} & \mathbf{0} \\ -\Omega & \overline{M} \end{bmatrix}, \qquad D = \begin{bmatrix} \alpha_x & \frac{l\alpha}{6}\overline{D} \\ \mathbf{0} & \end{bmatrix}, \\ \Lambda &= \begin{bmatrix} 0 & -\frac{AE}{l} & \mathbf{0} \\ \mathbf{0} & \overline{\Lambda} & \end{bmatrix}, \quad \Pi = \begin{bmatrix} 1 & \mathbf{0} \\ \mathbf{0} & \overline{\Pi} \end{bmatrix}, \end{aligned} \tag{6}$$

where $\alpha_x = 0.8$ is the friction added to the base to prevent unrealistic velocities during short contact-free durations. Because Equation 5 is now a linear time invariant ODE, there exists a closed form solution for the state transition between points in time. We start by creating an equivalent augmented system

$$\begin{aligned} A &= \begin{bmatrix} \mathbf{0} & \mathbf{I} \\ -M^{-1}\Lambda & -M^{-1}D \end{bmatrix}, \quad B = \begin{bmatrix} \mathbf{0} \\ M^{-1}\Pi \end{bmatrix} \\ z &= \begin{bmatrix} x_0 & \kappa & \dot{x}_0 & \dot{\kappa} \end{bmatrix}^\top \qquad F = \begin{bmatrix} f_a & \overline{F} \end{bmatrix}^\top \\ \dot{z} &= Az + BF \end{aligned} \tag{7}$$

Given a fixed time step Δt, we have a way to transition between an initial state $z(t)$ to the future state $z(t+\Delta t)$ along with a the force input F, by finding the homogeneous state transition and input matrix

$$\begin{aligned} &\Phi(\Delta t) = \exp(\Delta t A) \\ &\beta(\Delta t) = \int_0^{\Delta t} \exp(\Delta t - \tau) d\tau B = \begin{bmatrix} \mathbf{I} \\ \mathbf{0} \end{bmatrix}^\top \exp \begin{bmatrix} \Delta t A & B \\ \mathbf{0} & \mathbf{0} \end{bmatrix} \begin{bmatrix} \mathbf{0} \\ \mathbf{I} \end{bmatrix} \\ &z(t+\Delta t) = \Phi(\Delta t) z(t) + \beta(\Delta t) F(t). \end{aligned} \tag{8}$$

The matrices Φ and β can be precomputed for the time step $\Delta t = 0.001$ s for the duration of the simulation.

B. Contact dynamics

Coming up with a contact model first requires having a volumetric model of the nasal cavity. The basis of the volumetric model was taken as the mean nasal cavity STL file from Keustermans *et al.* [15]. However, a number of additional processing steps were needed to make it suitable as a collision volume. The original file represents the airway of the nasal cavity, so the convex hull was added to the surfaces to derive tissue boundaries. The nostrils are hollowed out by taking the boolean difference with a cylinder. Finally, the tetrahedral mesh of the cavity, for detecting swab vertices in collision, was derived using the TetWild program by Hu *et al.* [20] This process could be applied to other nasal cavity airways, although some manual intervention is needed to hollow out the nostrils.

If we let the nasal cavity's tetrahedral mesh and surface be represented with $\mathcal{N}$, the purpose of the collision model is to compute the forces $\overline{F}$ that are applied to the swab as a result of these collisions. In this work, we will consider that the collision response forces will be the result of a linear elastic model with Coulomb friction. This results in a number of assumptions, for computational reasons:

1) First, deformation of the surfaces of the nasal cavity is not explicitly modelled in simulation. Instead, the nasal cavity acts as a stationary force-field to repel the swab when it collides. Modelling tissue deformation would increase the number of states by many orders of magnitude. This would significantly slow down the simulation and collision detection and would also require having detailed knowledge of the tissue types (mucosa, bone, and cartilage).
2) Second, viscous friction was not modelled. In reality, the tissue has viscoelastic properties such that the force scales with the velocity. But this caused issues from numerical stiffness that currently prevented its inclusion in the model.

The points of collision were detected between the vertices of the swab's volume and the nasal cavity using a customized axis-aligned bounding box tree. When a collision is detected, a response force is applied on the i^{th} node of the beam as the sum of the spring's restitution force and the frictional force

$$F(x_i) = F_R(x_i) + F_F(x_i). \tag{9}$$

The restitution force is proportional to the distance of penetration with the solid, and directed back towards the nearest surface:

$$F_R(x_i) = -\lambda p(x_i), \tag{10}$$

where $p(x_i)$ is the vector of penetration. The spring constant λ is derived by taking into context the Young's modulus of elasticity E_t to reflect mucosa tissue that lines that nasal cavity. While there is limited sources detailing the physical properties of nasal mucosa, Chen *et al.* [21] surveyed physical properties of oral mucosa and found a wide variety of different moduli were in use. From this, we take $E_t = 10^6$ Pa. Deriving the spring constant we take $\lambda = \frac{E_t}{A} l_t$ where A is the cross section area of the beam and $l_t = 0.5$ mm is the base length of the spring.

Coulomb friction is implemented to resist motion perpen-

dicular to the restitution force

$$
\begin{aligned}
F_F(x_i) &= -\mu ||F_R(x_i)|| \nu_i, \\
\bar{\nu}_i &= \dot{\chi}_i - \dot{\chi}_i^\top \left(\frac{p(x_i)}{||p(x_i)||} \right) \left(\frac{p(x_i)}{||p(x_i)||} \right), \\
\nu &= \frac{\bar{\nu}}{||\bar{\nu}||}
\end{aligned}
\tag{11}
$$

with ν as a unit vector that is directed towards the component of node i's velocity that is perpendicular to the restitution force. The friction coefficient $\mu = 0.213$ was taken based on denture-mucosa contact [21], although it is unclear how applicable this value will be for NPS contact.

III. Optimization

With the beam-nasal cavity simulation formulated, we will now describe an optimization problem to find good trajectories to move the beam through the nasal cavity. As mentioned in subsection II-A, we will consider a control scenario where the base of the swab is moved along a linear trajectory, parameterized by a line segment (s,e), by applying a constant force f_a, where s is the point on an ellipse $\mathcal{S}$ on the nostril, where the head of the swab starts at, and e is the point on the ellipse $\mathcal{E}$ where the target nasopharynx region is. The three variables s, e, f_a are therefore the inputs to the simulation.

Along with reaching the nasopharynx, one aspect we want to minimize during the swab insertion is patient discomfort from the swab impacting the tissue. We quantify this as an objective by computing the amount of strain potential energy that the beam stores as it deforms from collisions with the nasal cavity during the simulation. Any necessary strain from collecting samples on the nasopharynx is disregarded because this occurs after insertion. Therefore, the averaged strain potential energy during the simulation, $\frac{1}{T}\int_0^T U dt$, is used as an objective in the optimization problem to seek trajectories that result in low deformation of the beam. Within the finite element model outlined in subsection II-A, the strain potential energy for a beam state is

$$
\begin{aligned}
U &= \frac{1}{2} E \int_0^L \left(A \left(\frac{\partial s}{\partial x} \right)^2 + I_z \left(\frac{\partial^2 v}{\partial x^2} \right)^2 + I_y \left(\frac{\partial^2 w}{\partial x^2} \right)^2 \right) dx \\
U &= \kappa^\top Q \kappa.
\end{aligned}
\tag{12}
$$

The energy matrix Q comes from assembly of the strain potential energy between adjacent FEM nodes for components s, v, and w respectively:

$$
\begin{aligned}
Q_s &= \frac{EA}{2l} \begin{bmatrix} 1 & -1 \\ -1 & 1 \end{bmatrix} \\
Q_v &= \frac{EI_z}{l^3} \begin{bmatrix} 12 & 6l & -12 & 6l \\ 6l & 4l^2 & -6l & 2l^2 \\ -12 & -6l & 12 & -6l \\ 6l & 2l^2 & -6l & 4l^2 \end{bmatrix} \\
Q_w &= \frac{EI_y}{l^3} \begin{bmatrix} 12 & 6l & -12 & 6l \\ 6l & 4l^2 & -6l & 2l^2 \\ -12 & -6l & 12 & -6l \\ 6l & 2l^2 & -6l & 4l^2 \end{bmatrix}.
\end{aligned}
\tag{13}
$$

Algorithm 1 is written to simulate the beam-cavity interaction scene initialized with trajectory (s,e) and applied force f_a, ultimately returning the average strain energy that occurs during simulation or a penalty if the nasopharynx is not reached within a time limit. On top of this, COBYLA [22] is applied to algorithm 1 to optimize over the trajectory path (s, e). COBYLA was chosen over derivative based optimizers because the large number of states and function evaluations that occur during the optimization makes computing derivatives with respect to the inputs infeasible. The applied force f_a is fixed during the optimization.

Algorithm 1: sim(s,e,f_a)

Set axis $\hat{\mathbf{i}} = \frac{e-s}{||e-s||}$;
Initialize $z = \mathbf{0}$;
t = 0.0;
energy = 0.0;
contact = false;
while *!contact and* $t <$ *time_limit* **do**
    energy = energy + $\Delta t * \kappa^\top Q \kappa$ /* Equation 12 */
    $\overline{F}$ = compute_collision_forces($\mathcal{N}$, z) /* (Equation 10 & 11) */
    $F = (f_a, \overline{F})$;
    $z = \Phi(\Delta t) z + \beta(\Delta t) F$; // Equation 8
    $t = t + \Delta t$;
    contact = check_nasopharynx_contact(z, $\mathcal{N}$) ; /* true if swab head reaches nasopharynx */
if *contact* **then**
    return energy/t;
else
    return 1000.0 // failure penalty

IV. Results & Discussion

Before examining the optimized trajectory outputs from applying section III, it is useful to examine how the magnitude of the applied force f_a affects the success rate of the swab reaching the nasopharynx, within a time limit of 7 s. We performed 4000 simulations while sampling on $s \in \mathcal{S}, e \in \mathcal{E}, f_a \in [0.001 \text{ N}, 0.2 \text{ N}]$. Figure 3 shows that increasing f_a increases the chances of a randomized trajectory reaching the nasopharynx, up until about 0.05 N after which there is little change. This indicates that increasing the applied force can allow the swab to overcome the collisions that occur in the nasal cavity. However, Figure 4 shows that the trade-off of increasing f_a is that the response forces applied to the swab increase as well. This is an important to note because these higher levels of force will cause a greater impact on the tissue that could presage patient discomfort.

Next, the COBYLA [22] algorithm optimized the outputs of algorithm 1 with $f_a \in \{0.02,0.04,0.06,0.08,0.10,0.12,0.14,0.16,0.18\}$. Overall, the optimization was quite successful in terms of finding

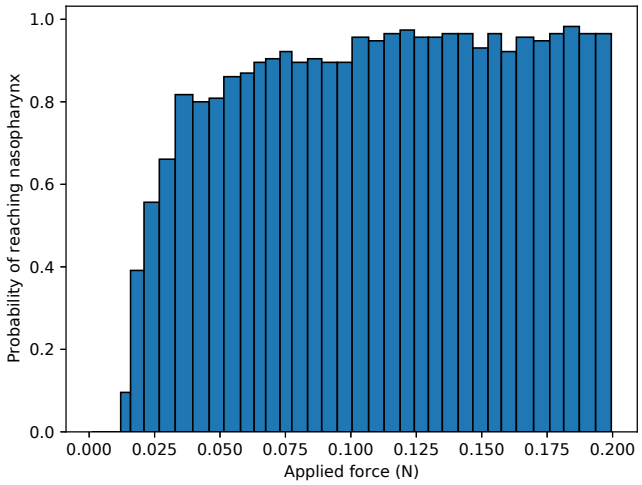

Fig. 3: Bar plots showing the probability of a randomized trajectory reaching the nasopharynx with respect to the applied force.

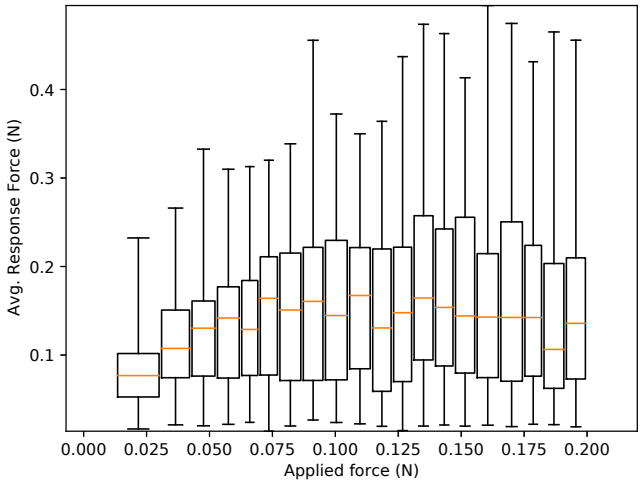

Fig. 4: Box plots showing the distribution of the average response collision forces with respect to applied force. Boxes extend one quartile from the median, whiskers span the rest of the range.

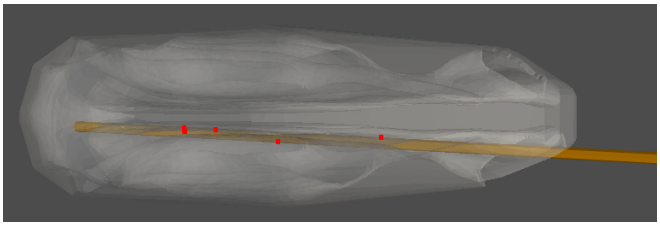

Fig. 5: Top view rendering of the swab (orange) inserted into the nasal cavity after following the COBYLA optimized trajectory using $f_a = 0.08$ N. Even in this optimized trajectory that results in minimal deformation, some collisions still occur (red).

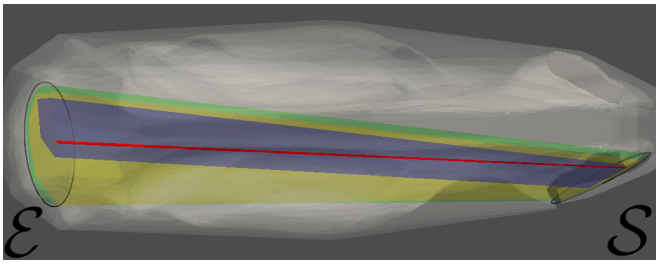

(a) Top view

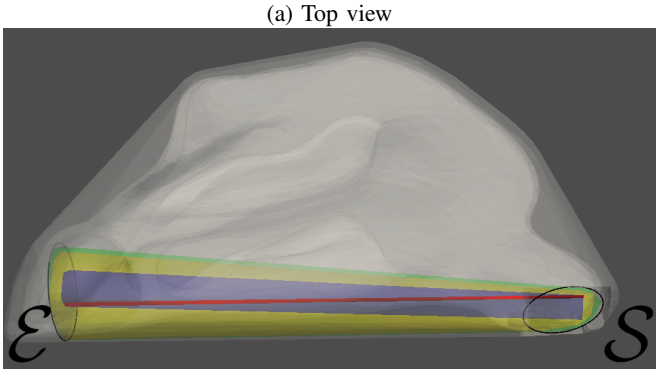

(b) Side view

Fig. 6: Convex hulls were taken of the pairs of points $s \in \mathcal{S}$ and at $e \in \mathcal{E}$ whose trajectories successfully reached the nasopharynx. The red hull shows the set of optimized paths found by COBYLA. The blue, yellow, and green hulls belong to trajectories that were able to reach the nasopharynx for $f_a \leq 0.015$, 0.025, and 0.05 Newtons respectively.

trajectories that minimized energy, with strain energy values in the range of 1.6×10^{-5} J to 3.0×10^{-4} J. The average trajectory had a pitch angle $0.25°$ down, with a yaw angle $1.63°$ towards the septum, located 4.68 mm from the columella (about one-third the distance to the ala). Figure 5 shows a rendering of the swab within the nasal cavity. Even in this optimized insertion, contact with the intermediate nasal cavity is inevitable, which causes some small amounts of strain on the swab. Figure 6 shows the span of the optimized trajectories through the nasal cavity, among the spans of other non-optimized trajectories that reached the nasopharynx at different force intervals. The figure shows that the optimized trajectories converged to similar paths over the set of different forces. The pitch angle of the paths seem to match clinical advice [4] [6] in the sense that the swab is angled parallel to the palate. In terms of yaw the swab is angled slightly inwards from the nostril towards the nasal septum, which largely allows it to avoid making contact with the adjacent inferior turbinate. Also plotted in Figure 6 are the spans for the trajectories in the upper bounds of f_a at 0.015, 0.025, and 0.05 Newtons, showing how the set of feasible trajectories through the nasal cavity expands as more force is applied.

A deeper analysis of the optimized trajectory can be found by examining the change in strain potential energy objective as the trajectory is perturbed from the optimal trajectory (s^*, e^*) (c.f. Figure 7). In Figure 8, the contour plots of

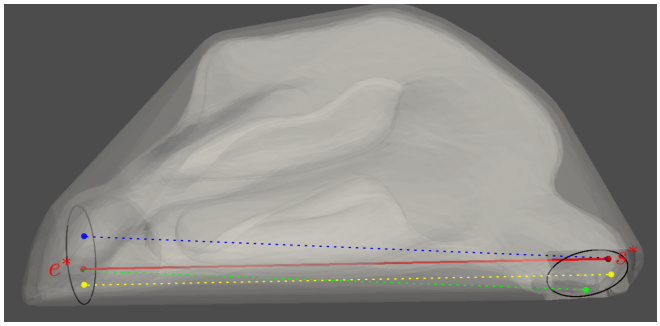

Fig. 7: Spatial representation of how the optimal trajectory (red) was perturbed to achieve the contour plots in Figure 8). Blue shows rotation about s^* (Figure 8a). Green shows rotation about e^* (Figure 8b). Yellow shows translation (Figure 8c).

the strain potential energy display this for $f_a = 0.08$ N. Figure 8a was found by rotation about s^*, while Figure 8b was found by rotation about e^*. In the former case, there is slightly less sensitivity to downward pitch, whereas changes in yaw cause issues by hitting the septum or the nasal vestibule wall. The latter case appears to be more sensitive to positive yaw, which leads to contact with the nasal vestibule and inferior turbinates. In contrast, Figure 8c shows the effect of keeping the same angle of insertion, but translating the entire trajectory in the transverse directions. Here, the objective rises steepest with horizontal translation towards the exterior of the cavity, where it will encounter the nasal vestibule wall and inferior turbinate. Overall, these plots show that the objective function has a steep well at the optimum found by COBYLA that rises with small changes of angle or position; rising several orders of magnitude in less than a degree or within 2 mm. Of course, this trajectory is optimized for this single nasal cavity. In reality, anatomical variations and hardware limitations will make achieving this best-case scenario unlikely.

Finally, it should be noted that the presented control scenario used in the simulation is simplified in a couple of ways. We showed that once the swab enters the nasal cavity, pushing it along a linear path is feasible for reaching the nasopharynx. However, some deviation may be needed in practice to enter the cavity amidst different external nostril shapes. We also assumed that constant force is applied to the base of the swab. In reality a controller would need to balance force and kinematic feedback as the swab encounters different forms of contact.

V. Conclusion

In this work, we developed a model to simulate the interaction between a swab and nasal cavity for nasopharyngeal swab insertion. Leveraging this simulation, we formulated an optimization problem to find an optimal insertion trajectory of 0.25° pitch down, 1.63° yaw inwards, located about one-third between the centre and edge of the nostril. We found that trajectories got significantly worse when perturbed

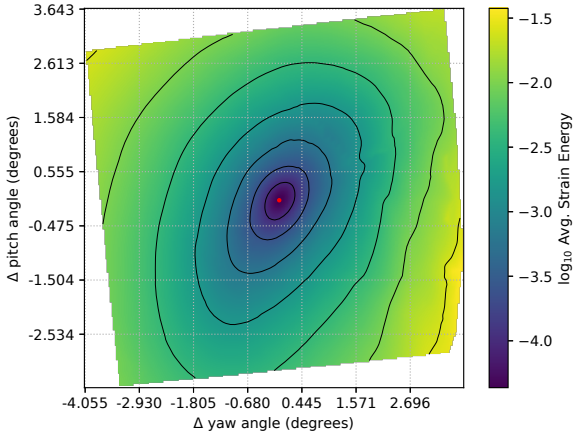

(a)

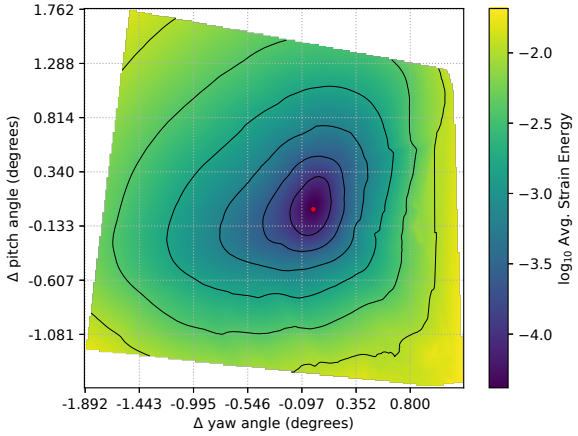

(b)

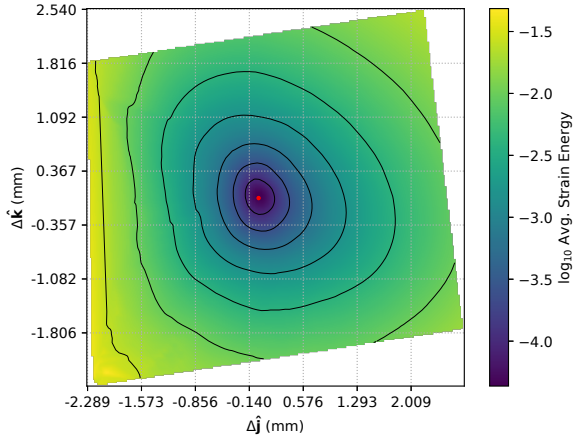

(c)

Fig. 8: Contour plots showing the change in objective function as perturbations are made about the optimal trajectory, parameterized by the line segment (s^*,e^*), found by COBYLA (annotated with a red dot). Fig. a) perturbs the trajectory by rotation about s^*. Fig. b) perturbs the trajectory by rotation about e^*. Fig. c) perturbs the trajectory through translation. A total of 6400 points were considered for each plot and filled in with linear interpolation; any points that did not reach the nasopharynx were excluded.

away from the optimum. Despite this we found that many non-optimal trajectories could still reach the nasopharynx provided sufficient force was applied to overcome collisions.

There are a number of potential avenues for future work. As this is our initial work, we only used a single nasal cavity model for the simulations. We would like to extend our work to a variety of different nasal cavity shapes to better study insertion trajectories over the population as a whole. This would include investigating how nasal cavity abnormalities, such as deviated septums, affect the procedure. Another area to build on would be adding viscosity properties to the nasal tissue. Simulating the impact of inflamed tissue and its impact on the insertion would also be of particular interest because this could be a common symptom of ill patients who are in need of these tests. Finally, simulation of the latter collection and extraction phases and the transitions between the three phases will be considered.

As mentioned in the introduction, a primary motivation of modelling the swab-cavity interaction is for use robotic control. In the physical world, a robot would need to have an intricate controller that can balance responding to disturbances like motion and variance in anatomy and observing safety criteria, while also following a baseline trajectory and responding to the expected interaction forces. Our work helps for planning this baseline trajectory through the nasal cavity, with possible extensions of evaluating control systems in the proposed simulation environment.

ACKNOWLEDGMENT

We acknowledge the support of the Natural Sciences and Engineering Research Council of Canada (NSERC), from the Tri-Agency Canada Excellence Research Chair Program, and from the University of Waterloo.

REFERENCES

[1] A. Kritikos, G. Caruana, R. Brouillet, J.-P. Miroz, S. Abed-Maillard, G. Stieger, O. Opota, A. Croxatto, P. Vollenweider, P.-A. Bart, J.-D. Chiche, and G. Greub, "Sensitivity of rapid antigen testing and RT-PCR performed on nasopharyngeal swabs versus saliva samples in COVID-19 hospitalized patients: Results of a prospective comparative trial (RESTART)," *Microorganisms*, vol. 9, no. 9, 2021.

[2] B. Clerici, A. Muscatello, F. Bai, D. Pavanello, M. Orlandi, G. C. Marchetti, V. Castelli, G. Casazza, G. Costantino, and G. M. Podda, "Sensitivity of SARS-CoV-2 detection with nasopharyngeal swabs," *Frontiers in Public Health*, vol. 8, p. 1098, 2021.

[3] A. L. Leber, J. G. Lisby, G. Hansen, R. F. Relich, U. V. Schneider, P. Granato, S. Young, J. Pareja, I. Hannet, and Y.-W. Tang, "Multicenter evaluation of the qiastat-dx respiratory panel for detection of viruses and bacteria in nasopharyngeal swab specimens," *Journal of Clinical Microbiology*, vol. 58, no. 5, pp. e00 155–20, 2020.

[4] A. Piras, D. Rizzo, E. Longoni, N. Turra, S. Urru, P. P. Saba, L. Musumano, and F. Bussu, "Nasopharyngeal swab collection in the suspicion of Covid-19," *American Journal of Otolaryngology*, vol. 41, no. 5, p. 102551, 2020.

[5] N. M. Hiebert, B. A. Chen, and L. J. Sowerby, "Variability in instructions for performance of nasopharyngeal swabs across Canada in the era of COVID-19 – what type of swab is actually being performed?" *Journal of Otolaryngology - Head & Neck Surgery*, vol. 50, no. 1, p. 5, Jan 2021.

[6] F. M. Marty, K. Chen, and K. A. Verrill, "How to obtain a nasopharyngeal swab specimen," *New England Journal of Medicine*, vol. 382, no. 22, p. e76, 2020.

[7] "How to obtain a nasopharyngeal swab specimen," 2020. [Online]. Available: https://doi.org/10.1056/NEJMc2015949

[8] H. Christensen, N. Amato, H. Yanco, M. Mataric, H. Choset, A. Drobnis, K. Goldberg, J. Grizzle, G. Hager, J. Hollerbach, S. Hutchinson, V. Krovi, D. Lee, B. Smart, J. Trinkle, and G. Sukhatme, "A roadmap for US robotics from internet to robotics 2020 edition," 2020.

[9] H. Zhang, Q. Wang, C. Chi, Y. Chen, Z. Mu, Z. Li, Y. Lan, and A. Zhang, "Design and implementation of a novel, intrinsically safe rigid-flexible coupling manipulator for COVID-19 oropharyngeal swab sampling," in *2021 IEEE International Conference on Robotics and Automation (ICRA)*, 2021.

[10] S. Wang, K. Wang, H. Liu, and Z. Hou, "Design of a low-cost miniature robot to assist the COVID-19 nasopharyngeal swab sampling," *CoRR*, vol. abs/2005.12679, 2020.

[11] C. Duriez, C. Guébert, M. Marchal, S. Cotin, and L. Grisoni, "Interactive simulation of flexible needle insertions based on constraint models," in *Medical Image Computing and Computer-Assisted Intervention – MICCAI 2009*, 2009.

[12] C. Yang, Y. Xie, S. Liu, and D. Sun, "Force modeling, identification, and feedback control of robot-assisted needle insertion: A survey of the literature," *Sensors*, vol. 18, no. 2, 2018.

[13] K. Sathirakul and R. H. Sturges, "Jamming conditions for multiple peg-in-hole assemblies," *Robotica*, vol. 16, no. 3, p. 329–345, May 1998.

[14] J. Xu, Z. Hou, Z. Liu, and H. Qiao, "Compare contact model-based control and contact model-free learning: A survey of robotic peg-in-hole assembly strategies," *CoRR*, vol. abs/1904.05240, 2019.

[15] W. Keustermans, T. Huysmans, F. Danckaers, A. Zarowski, B. Schmelzer, J. Sijbers, and J. J. J. Dirckx, "High quality statistical shape modelling of the human nasal cavity and applications," *Royal Society Open Science*, vol. 5, no. 12, p. 181558, 2018.

[16] O. A. Bauchau and J. I. Craig, *Three-dimensional beam theory*. Springer Netherlands, 2009, pp. 223–259.

[17] S. Timoshenko, "Lxvi. on the correction for shear of the differential equation for transverse vibrations of prismatic bars," *Taylor & Francis*, vol. 41, no. 245, pp. 744–746, 1921.

[18] H. Zohoor and F. Kakavand, "Vibration of Euler–Bernoulli and Timoshenko beams in large overall motion on flying support using finite element method," *Scientia Iranica*, vol. 19, no. 4, pp. 1105–1116, 2012.

[19] J. Chung and H. Yoo, "Dynamic analysis of a rotating cantilever beam by using the finite element method," *Journal of Sound and Vibration*, vol. 249, no. 1, pp. 147–164, 2002.

[20] Y. Hu, Q. Zhou, X. Gao, A. Jacobson, D. Zorin, and D. Panozzo, "Tetrahedral meshing in the wild," *ACM Trans. Graph.*, vol. 37, no. 4, Jul 2018.

[21] J. Chen, R. Ahmad, W. Li, M. Swain, and Q. Li, "Biomechanics of oral mucosa," *Journal of The Royal Society Interface*, vol. 12, no. 109, p. 20150325, 2015.

[22] M. J. D. Powell, *A Direct Search Optimization Method That Models the Objective and Constraint Functions by Linear Interpolation*. Springer Netherlands, 1994, pp. 51–67.